International Journal of Solids and Structures 50 (2013) 1055–1066

Contents lists available at SciVerse ScienceDirect

International Journal of Solids and Structures

journal homepage: www.elsevier.com/locate/ijsolstr

Predicting ductile fracture of low carbon steel sheets: Stress-based versus mixed stress/strain-based Mohr–Coulomb model

Fabien Ebnoether [a], Dirk Mohr [a,b,*]

[a] Solid Mechanics Laboratory (CNRS-UMR 7649), Department of Mechanics, École Polytechnique, Palaiseau, France
[b] Impact and Crashworthiness Laboratory, Department of Mechanical Engineering, Massachusetts Institute of Technology, Cambridge, MA, USA

ARTICLE INFO

Article history:
Received 18 May 2012
Received in revised form 29 October 2012
Available online 27 December 2012

Keywords:
Ductile fracture
Finite element model
Commercial steel
Non-associated plasticity
Stress triaxiality
Mohr–Coulomb failure criterion

ABSTRACT

Two distinct implementations of the Mohr–Coulomb failure model are used in conjunction with a non-associated quadratic plasticity model to describe the onset of fracture in low carbon steel sheets. The stress-based version corresponds to the original Mohr–Coulomb model in stress space. For the mixed stress/strain-based version, the Mohr–Coulomb failure criterion is first transformed into the space of stress triaxiality, Lode angle parameter and equivalent plastic strain and then used as stress-state dependent weighting function in a damage indicator model. Basic fracture experiments including tensile specimens of different notch radii and a punch test are performed to calibrate the material parameters of the respective models. Subsequently, the models are used to predict the crack initiation in a Hasek test and during the stamping of an anticlastic structure. Unlike for the calibration experiments, the loading history during stamping is highly non-linear. Both models can be calibrated with similar accuracy, but the strain-based model predicts the instant of onset of fracture with greater accuracy in the stamping experiment which is an advantage of the empirical damage accumulation rule.

1. Introduction

The prediction of failure during sheet metal forming is an important step throughout the virtual design of thin-walled structures. Forming Limit Diagrams (FLDs) are typically used to predict the onset of through-thickness necking (e.g., Keeler and Backofen, 1963). The FLD describes the limiting strains in terms of major and minor in-plane strains. Several analytical and numerical models have been developed to predict the FLDs (e.g., Hill, 1952; Swift, 1952; Marciniak and Kuczynski, 1967). The Marciniak–Kuczynski (MK) model assumes a small region of thickness imperfection and provides an estimate of the FLD for positive and negative minor strains, while Hill's analytical model can only be used for negative minor strains. Alternatively, the FLD may be determined experimentally using multi-axial experiments such as Hasek or Nakazima tests. Conventional FLDs are strain-based and describe the onset of necking for monotonic proportional loading paths only. It is well-known that the strain-based FLD changes substantially if the loading path is non-linear (e.g., Kleemola and Pelkki-kangas, 1977). To address this issue, stress-based FLDs have been proposed (e.g., Stoughton, 2000) which provide better estimates of the formability limits for non-proportional loading than conventional strain-based FLD's.

In some applications, sheet material structures are designed up to the point of onset of fracture. In other words, the material's ability to deform after the onset of through-thickness necking is taken into account. In some rare (but important) cases, fracture may occur before the onset of necking. In both cases, a reliable ductile fracture model is needed. There exists a wealth of models that have been developed based on the assumption that ductile fracture is the result of the nucleation, growth and coalescence of voids. The early investigations of McClintock (1968) and Rice and Tracey (1969) on the evolution of cylindrical and spherical holes in ductile matrices have set the foundation for numerous studies on the micromechanics associated with void growth. The most prominent is that of Gurson (1977), who proposed a porous plasticity model based on the micromechanical analysis of a thick spherical shell subject to hydrostatic pressure. The original Gurson model has been repeatedly modified to account for additional processes responsible for microstructural evolution and subsequent ductile fracture: void nucleation (e.g., Chu and Needleman, 1980), loss of load-carrying capacity associated with void coalescence (e.g., Tvergaard and Needleman, 1984), enhanced strain hardening models (e.g., Leblond et al., 1995), void shape effects (e.g., Gologanu et al., 1993, 1994; Garajeu et al., 2000; Pardoen and Hutchinson, 2000) and plastic anisotropy (e.g., Benzerga et al., 2004). The reader is referred to Lassance et al. (2007), Benzerga and Leblond (2010)

* Corresponding author at: Solid Mechanics Laboratory (CNRS-UMR 7649), Department of Mechanics, École Polytechnique, Palaiseau, France. Tel.: +33 1 69 33 58 01.
E-mail address: mohr@mit.edu (D. Mohr).

0020-7683/$ - see front matter © 2012 Elsevier Ltd. All rights reserved.
http://dx.doi.org/10.1016/j.ijsolstr.2012.11.026

and Besson (2010) for a comprehensive review of successive improvements of the Gurson model. The latter review also covers continuum damage mechanics (CDM) models based on the work of Lemaitre (1985) which are not addressed here. Recent works on Gurson-type of models deal with its modification for shear-dominated loading (Xue, 2008; Nahshon and Hutchinson, 2008; Nielsen and Tvergaard, 2010). Models for porous solids based on non-linear homogenization have also been proposed (e.g., Ponte Castaneda and Zaidman, 1994; Danas et al., 2008; Danas and Ponte Castaneda, 2009a,b). Defining the onset of fracture through peak load or loss of ellipticity, homogenization models provide valuable insight into the effect of stress triaxiality and Lode angle on the onset of fracture (Danas and Ponte Castaneda, 2012).

Phenomenological and empirical damage indicator models are particularly popular in engineering practice. Unlike in Gurson, CDM, and homogenization based models, the models describing the evolution of plasticity and damage are uncoupled. Most uncoupled fracture/damage models are formulated in the space of stress-triaxiality, Lode angle and equivalent plastic strain. The most basic models (McClintock, 1968; Rice and Tracey, 1969; Hancock and Mackenzie, 1976; Johnson and Cook, 1985; LeRoy et al., 1981; Oh et al., 1979; Brozzo et al., 1972; Clift et al., 1990) neglect the effect of loading path in that space and define the equivalent plastic strain at the onset of fracture as an explicit function of the stress triaxiality. Such models can also be integrated into a damage indicator framework (e.g., Fischer et al., 1995), where an empirical damage variable is defined by the integral of a stress-state dependent weighting function along the equivalent plastic strain path. Successful applications of the model by Cockcroft and Latham (1968) are found in Borvik et al. (2009) and Fagerholt et al. (2010). Bao and Wierzbicki (2004a) published a comparative study on these models using the inverse of the above definitions of the strain to fracture as weighting functions. The recent experimental observation of a non-smooth fracture locus in the plane of fracture strain versus stress triaxiality (Bao and Wierzbicki, 2004a,b; Barsoum and Faleskog, 2007) revived the discussions of the possible effect of the Lode angle on the onset of fracture in metals. Phenomenological models accounting for the effect of the Lode angle have been proposed e.g., by Bao and Wierzbicki (2004a,b); Bai and Wierzbicki (2008), Coppola et al. (2009), Xue et al. (submitted)). Recent studies comparing the predictive capabilities of phenomenological, Gurson and CDM models can be found in Dunand and Mohr (2011), Li et al. (2011) and Malcher et al. (2012). The conclusions from these comparative studies are not consistent which is possibly due to experimental uncertainties, an effect of the investigated alloy, and some user influence on the model calibration.

The damage indicator model by Bai-Wierzbicki model is formulated in the above space of equivalent plastic strain, stress triaxiality and Lode angle parameter, but has been derived from the Mohr–Coulomb model in stress space. Closing the loop with discussions in the 1920s (e.g., Lode, 1926), two recent papers suggest criteria in stress space to predict ductile fracture. Stoughton and Yoon (2011) revisited the experimental data on bulk Al2024-T351 reported by Wierzbicki et al. (2005) to advocate a maximum shear stress criterion for predicting ductile fracture (which includes the Mohr–Coulomb and Tresca model). Khan and Liu (2012) supplemented the data of Wierzbicki et al. (2005) with experimental results for free-end torsion, torsion with constant tension, and biaxial compression in a channel-die; they proposed an empirical stress criterion which expresses the maximum magnitude of the principal stress vector as a function of a first-order polynomial function of the first stress tensor invariant.

The purpose of the present work is to compare the predictive capabilities of a conventional Mohr–Coulomb criterion in stress space (stress-based model) and a damage indicator model (mixed stress/strain-based model) with a stress-state dependent weighting function that has been derived from the original Mohr–Coulomb criterion. Our attention is limited to a rather narrow, but important range of nearly plane stress states between uniaxial and equi-biaxial tension. Tension and punch experiments are performed on notched specimens extracted from thin low carbon steel sheets. The large deformation behavior is described through a quadratic plasticity model with isotropic hardening and non-associated flow rule (Mohr et al., 2010). The two parameters (friction coefficient and cohesion) of the respective stress-based and mixed stress/strain-based models are subsequently identified using a hybrid experimental-numerical inverse identification procedure. The models are then used to predict the onset of fracture in a Hasek test as well as in a complex forming experiment of an anticlastic structure with highly non-linear loading paths. It is found that the Mohr–Coulomb fracture model provides better estimates of the instant of onset of fracture during stamping when it is embedded in a damage indicator framework as opposed to its original stress-based version.

2. Material and plasticity model

2.1. Material

All specimens are extracted from 0.36 mm thick galvanized low carbon steel sheets. The thickness of the Commercial Steel (CS) Type B is achieved by a hot rolling process ($t_{sheet} \geqslant 1mm$) followed by cold rolling prior to hot dip galvanizing. The latter process adds 6 μm to each sheet surface according to the G30 coating designation. An average grain size of 5 to 10 μm has been estimated from a cross-section micrograph (Fig. 1). To visualize the grain boundaries, the polished surface has been etched using a 2% Nital solution.

The true stress-strain curves for uniaxial tension along three different material directions are shown in Fig. 2. The curves feature an upper yield stress followed by a lower yield stress plateau prior to monotonic strain hardening. This response is the characteristic signature of Lüders' bands which are also observed in the corresponding DIC strain field measurements (not shown). After onset of monotonic strain hardening, almost the same stress-strain response is measured for tension along the rolling and the diagonal direction, while the stress level is about 3% lower for the transverse specimen. The plastic strains are determined assuming a Young's Modulus of $E = 200GPa$ and an elastic Poisson's ratio of $\nu = 0.3$. The corresponding Lankford ratios as determined from the average slopes of the logarithmic plastic width strain versus logarithmic

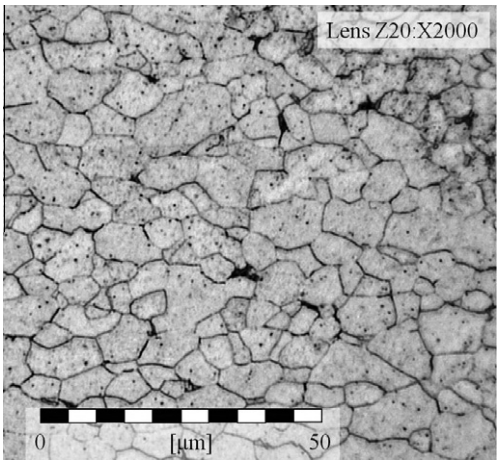

Fig. 1. Micrograph of the low carbon steel cross-section with etched grain boundaries (scale 5 μm).

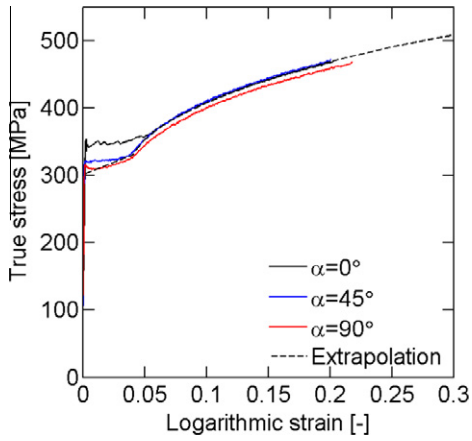

Fig. 2. Measured true stress versus logarithmic plastic strain curves for uniaxial tension along different in-plane directions (solid lines) and isotropic hardening law approximation (dashed line).

plastic thickness strain curves are $r_0 = 1.27$, $r_{45} = 0.96$ and $r_{90} = 1.05$.

2.2. Plasticity model

The direction-dependency of the r-values indicates planar anisotropy while the small differences among the stress-strain curves suggest a nearly planar isotropic material behavior (except for the Lüders plateau). A quadratic plane stress plasticity model with non-associated flow rule (Mohr et al., 2010) is therefore used to describe elasto-plastic behavior of the sheet material.

The model assumes a von Mises yield function,

$$f(\boldsymbol{\sigma}, k) = \bar{\sigma}_{vM} - k = 0, \tag{1}$$

where $\bar{\sigma}_{vM}$ denotes the equivalent von Mises stress,

$$\bar{\sigma}_{vM} = \sqrt{\frac{3}{2}\mathbf{s}\cdot\mathbf{s}} \quad \text{with } \mathbf{s} = \boldsymbol{\sigma} - \sigma_m\mathbf{1} \text{ and } \sigma_m = \frac{tr\boldsymbol{\sigma}}{3}. \tag{2}$$

$\boldsymbol{\sigma}$ is the Cauchy stress tensor in material coordinates, $\mathbf{s}$ the corresponding deviatoric stress tensor, and σ_h is the hydrostatic stress. The direction of plastic flow is assumed to be aligned with the stress derivative of a flow potential function $g(\sigma)$,

$$d\boldsymbol{\varepsilon}_p = d\lambda\frac{\partial g}{\partial \boldsymbol{\sigma}}, \tag{3}$$

where $d\boldsymbol{\varepsilon}_P$ denotes the plastic strain tensor increment in material coordinates; $d\lambda \geqslant 0$ is a scalar plastic multiplier. The potential function $g(\sigma)$ is defined as an anisotropic quadratic function in stress space

$$\begin{aligned} g^2(\boldsymbol{\sigma}) = {} & \sigma_{11}^2 + G_{22}\sigma_{22}^2 + (1 + 2G_{12} + G_{22})\sigma_{33}^2 + 2G_{12}\sigma_{11}\sigma_{22} \\ & - 2(1 + G_{12})\sigma_{11}\sigma_{33} - 2(G_{22} + G_{12})\sigma_{22}\sigma_{33} + G_{33}\sigma_{12}^2 \\ & + 3\sigma_{13}^2 + 3\sigma_{23}^2 \end{aligned} \tag{4}$$

with the anisotropy coefficients G_{22}, G_{12} and G_{33}. The above function corresponds to a special case of the Hill'48 function which accounts for the apparent planar anisotropy associated with the direction-dependency of the r-values.

Isotropic hardening is introduced into the model through the equation

$$k = k[\bar{\varepsilon}_p], \tag{5}$$

with the equivalent plastic strain defined as $\bar{\varepsilon}_p = \int d\lambda$.

2.3. Model calibration

The coefficients of the orthotropic flow potential function are determined from the r-values using the analytical relationships

$$\begin{aligned} G_{12} = -\frac{r_0}{1 + r_0}, \quad G_{22} = \frac{r_0}{r_{90}}\frac{1 + r_{90}}{1 + r_0} \quad \text{and} \quad G_{33} \\ = \frac{1 + 2r_{45}}{r_{90}}\frac{r_0 + r_{90}}{1 + r_0}. \end{aligned} \tag{6}$$

The strain hardening curve $k[\bar{\varepsilon}_p]$ is approximated by a piecewise linear function (Table 1, Fig. 2). The measured stress-strain curve is used up to the onset of necking (at an equivalent plastic strain of about 0.2). Note that the initial Lüders band dominated stress-strain response ($\bar{\varepsilon}_p < 0.005$) is not modeled in detail and is approximated by a monotonically increasing function instead. The strain hardening for large strains ($\bar{\varepsilon}_p > 0.2$) is determined through the inverse calibration with respect to the measured force-displacement curve of a specimen with a shallow notch ($R = 20$ mm, to be discussed in Section 3).

Fig. 3 compares the predicted and the measured engineering axial stress-strain curves and engineering width versus axial strain curves for the three material directions. For reference, the results are also shown for an isotropic and an anisotropic quadratic model with associated flow rule. Among the three models, the non-associated flow rule model clearly provides the most accurate description of the experimental results. Note that similar observations advocating the use of non-associated flow rules have been made by others (e.g., Stoughton and Yoon, 2004; Cvitanic et al., 2008; Mohr et al., 2010).

3. Hybrid experimental-numerical fracture characterization

A first set of fracture experiments is performed to *calibrate* the fracture models presented in the next section. The calibration experiments include the tensile testing of specimens of different notch radii and the punch testing of a disc specimen. A hybrid experimental-numerical approach is taken to determine the corresponding loading path to fracture in the space of stress triaxiality, Lode angle parameter and equivalent plastic strain.

The stress triaxiality is defined as the ratio of the mean and the von Mises stress,

$$\eta := \frac{\sigma_m}{\bar{\sigma}_{vM}} \tag{7}$$

while the Lode angle parameter $\bar{\theta}$ is related to the ratio of the third and second invariant of the deviatoric stress tensor,

$$\bar{\theta} := 1 - \frac{2}{\pi}\arccos\left(\frac{27}{2}\frac{\det(\mathbf{s})}{\bar{\sigma}_{vM}^3}\right). \tag{8}$$

Note that values of the Lode angle parameter always lie in the interval $[-1, 1]$. In a first approximation, the Lode angle parameter corresponds to the opposite of the original Lode parameter μ (Lode, 1926),

Table 1
Isotropic hardening law approximation.

$\bar{\varepsilon}_p$ (–)	0.00	0.04	0.05	0.06	0.07	0.08	0.1	0.12	0.14	0.16	0.2	0.25	0.3	1
k [MPa]	301fs	330	353	368	380	390.5	408	423	436	448	469	491	509	761

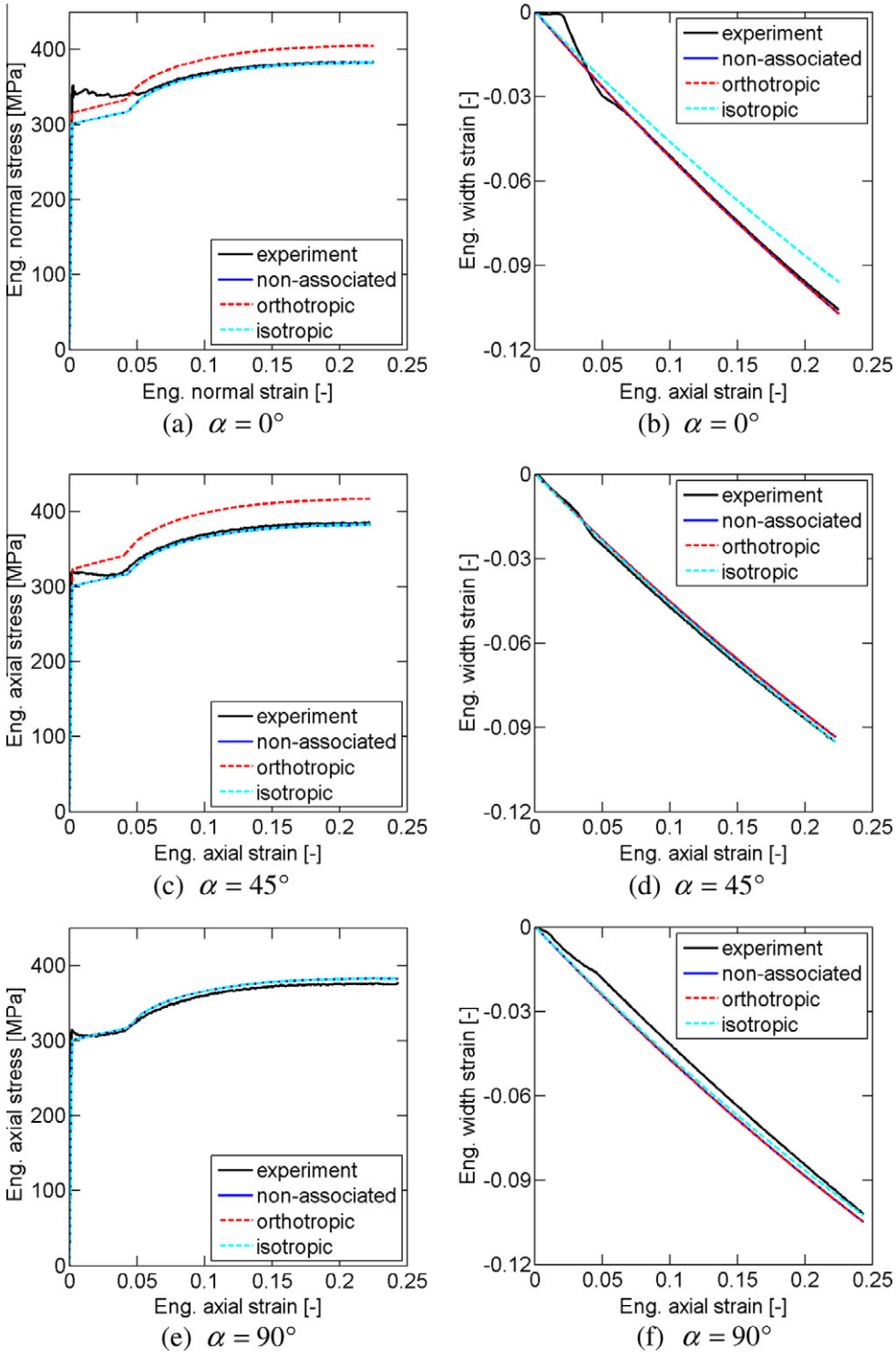

Fig. 3. Comparison of the effect of different plasticity model assumptions (von Mises with AFR, Hill with AFR, and von Mises with Hill FR) on the stress–strain response for different loading directions.

$$\bar{\theta} := \cong -\mu. \tag{9}$$

The limits $\bar{\theta} = 1$ and $\bar{\theta} = -1$ therefore correspond to axisymmetric tension (e.g., uniaxial tension) and axisymmetric compression (e.g., equi-biaxial tension), respectively. $\bar{\theta} = 0$ corresponds to generalized shear (e.g., pure shear or plane strain tension).

3.1. Experiments and simulations for notched tension

Following the basic fracture testing program proposed by Dunand and Mohr (2010), tensile specimens with the notch radii $R = 20$ mm, $R = 10$ mm and $R = 6.67$ mm are prepared (see Fig. 2 in Dunand and Mohr (2011) for technical drawings of the

specimens). The tensile axis of all specimens is aligned with the rolling direction. The specimens are mounted on a hydraulic testing machine (Model 8080, Instron, MA) and loaded under quasi-static loading conditions at a constant crosshead velocity of 0.5 mm/min. A 50kN load cell is used to record the axial force, while a DIC based optical extensometer is employed to measure the relative displacement of the specimens shoulders. A computer-controlled digital camera (QImaging Retiga 1300i with 85 mm Nikon Nikkor lenses) acquired about 400 photographs of the speckle painted front surface of the specimens during the tests. The camera is positioned at a distance of 1 m to monitor the entire specimen gage section (square pixel edge length of 56 μm). The average speckle size is about 200 μm. The displacement is calculated by DIC (VIC2D, Correlated Solutions) using a virtual extensometer of the window size 21 x 21 pixels and the step size of one pixel.

Fig. 4 shows the recorded force-displacement curves for the three different notched specimens all the way to fracture. Note that all curves exhibit a force maximum prior to crack initiation. Fracture is expected to initiate within the specimen mid-plane at the center of the specimen. Both strains and stresses cannot be measured directly at this location and a hybrid experimental-numerical approach is necessary. Exploring the symmetry of the mechanical system, only one eighth of the specimen is modeled. A uniform, constant velocity is assigned to the upper specimen shoulder, whereas zero normal displacement is imposed on the three boundary surfaces that correspond to symmetry planes. The required mesh density of four first-order solid elements along the half-thickness is determined with respect to convergence of the equivalent plastic strain estimates at the specimen center for the $R = 10mm$ notched tensile specimen.

Figs. 5a and 5b show the computed evolution of the equivalent plastic strain at the specimen center as a function of the Lode angle parameter and the stress triaxiality, respectively. All curves are in hierarchical order. The equivalent plastic strains to fracture are 0.36 for $R = 6.67mm$, 0.36 for $R = 10mm$ and 0.39 for $R = 20mm$. It is worth noting that the loading path for each experiment is non-linear in the space of stress triaxiality, Lode angle parameter and equivalent plastic strain; this is mainly attributed to the through-thickness necking of all notched specimens prior to fracture.

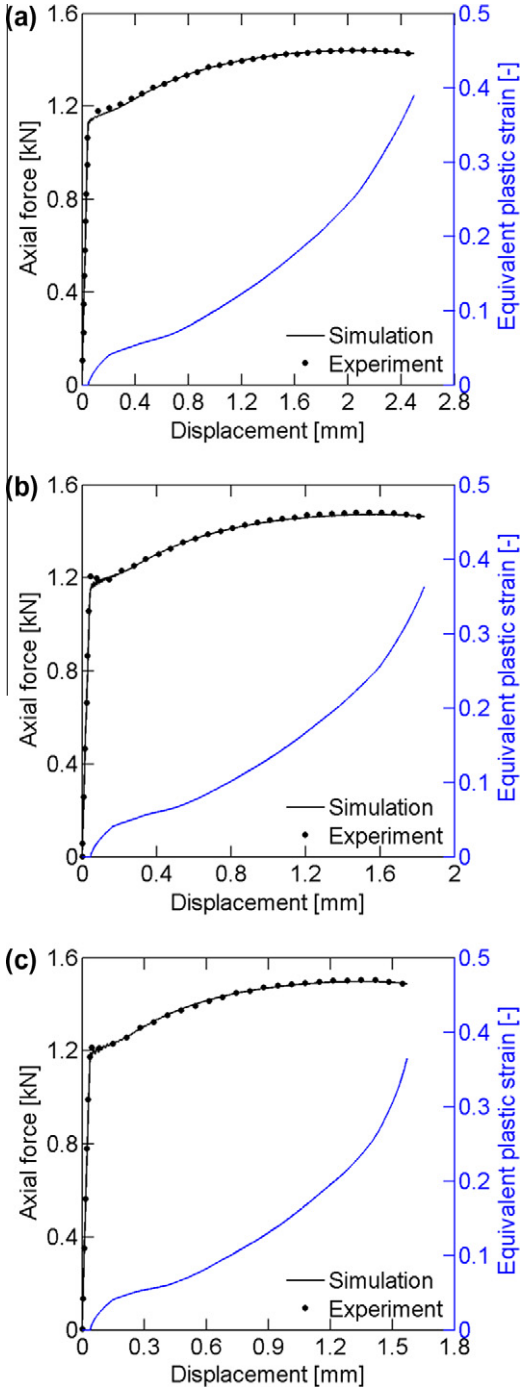

Fig. 4. Plots of the experimental and numerical results of the notched tensile specimens with (a) a cutout radius $R = 20$ mm, (b) $R = 10$ mm and (c) $R = 6.67$ mm.

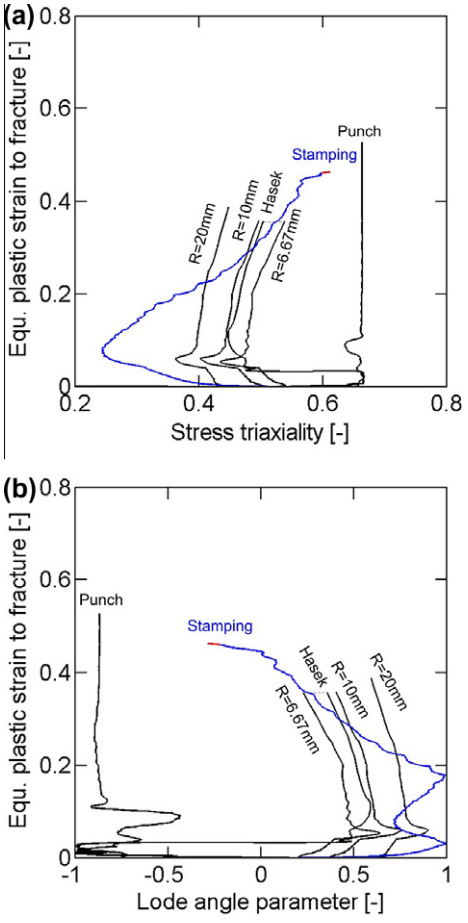

Fig. 5. Evolution of the equivalent plastic strain: (a) as a function of the stress triaxiality, (b) as a function of the Lode angle parameter.

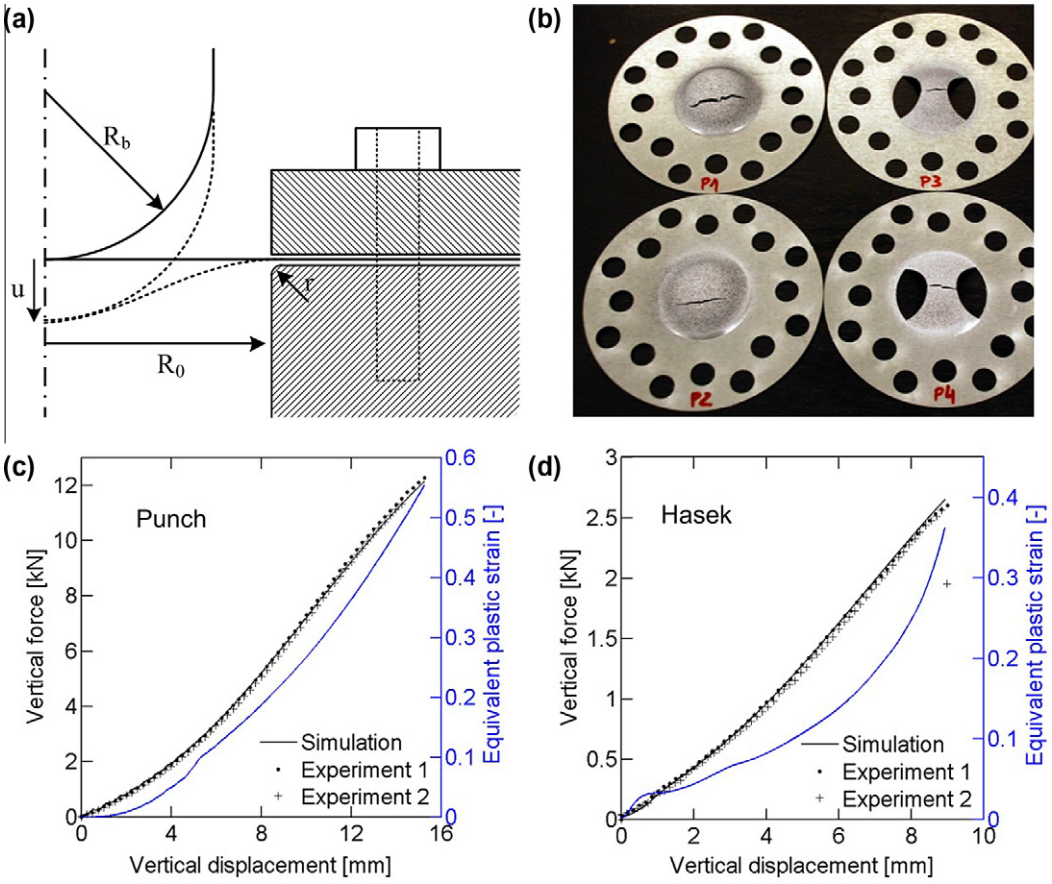

Fig. 6. (a) Schematic of set-up for punch experiments, (b) fractured punch and Hasek specimens; force–displacement curves for punch experiment on (c) a circular disc, (d) Hasek specimen.

3.2. Punch experiments

A disc specimen is clamped on a circular die (Fig. 6a) and monotonically loaded up to the point of fracture using a hemispherical punch. The circular die has an inner radius of $R_0 = 24.5mm$ and a die corner radius of $R = 1mm$. The clamping pressure is applied through sixteen (1/2)″-20 screws. For both experiments, a hemispherical punch of radius $R_b = 22.2mm$ loads the specimen at a constant velocity of 3 mm/min. A stack of four oil-lubricated 0.05 mm thick Teflon films is used to reduce friction between the specimen and the punch surface. Fig. 6c shows the respective measured force-displacement curves for two punch experiments. The corresponding fractured specimens are shown in Fig. 6b. A dramatic drop in force level is observed as a macroscopic crack becomes visible on the specimen surface. Note that the crack in the specimen does not initiate at the specimen center as the visible crack is located at a distance of about 8 mm from the apex of the punched specimen.

The corresponding finite element model comprises only one quarter of the specimen, whereas the clamping and loading system is modeled using analytical rigid surfaces. The geometry is meshed with linear, reduced-integration solid elements (C3D8R). The mesh featured eight elements through the thickness and an element size of $l_e = 100\mu m$ at the specimen center. The punch/sheet contact is modeled using a sliding contact model with a friction coefficient of 0.04, while neglecting the effective punch radius increase due to the Teflon layers. The evolution of the equivalent plastic strain and the stress state is plotted in Fig. 5 for the integration point of an element situated near the point of the observed crack. The corresponding estimated equivalent plastic strains at failure is 0.53 .

4. Mohr–Coulomb based fracture modeling

In sheet metal forming simulations, the plastic strain just outside the neck is often used to characterize failure (e.g., forming limit diagrams). Our goal on the other hand is to predict the onset of ductile fracture. Depending on the material and stress state, ductile fracture may occur before or after the necking limit. All simulations will thus be performed with eight first-order solid elements along the sheet thickness-direction to be able to approximate the stress and strain fields before and after necking. At the same time, Mohr–Coulomb based fracture models will be employed to predict ductile fracture.

The Mohr–Coulomb model had been proposed by Mohr (1900) to describe the failure of steels through a failure surface in stress space. Bai and Wierzbicki (2010) made use of this model as the starting point for the construction of a stress-state dependent damage indicator model. The latter formulation involves the partial transformation from stress to strain space. We thus differentiate between stress-based Mohr–Coulomb model which corresponds to its original version and a mixed stress/strain-based damage indicator version which will be developed below.

4.1. Stress-based Mohr–Coulomb fracture model

The Mohr–Coulomb failure surface is well-known in the form

$$\max_{\mathbf{n}}(\tau + c_1\sigma_N) = c_2 \tag{10}$$

with τ and σ_N denoting the respective shear and normal stresses acting on a plane of normal vector $\mathbf{n}$. The coefficients c_1 and c_2

are commonly referred to as the friction and cohesion of a material. As shown in Bigoni and Piccolroaz (2004), it can also be written in terms of the stress tensor invariants $\{\bar{\sigma}, \eta, \bar{\theta}\}$,

$$\bar{\sigma}_f = \frac{c_2}{\sqrt{\frac{1+c_1^2}{3}}\cos[\frac{\pi}{6}\bar{\theta}] + c_1(\eta + \frac{1}{3}\sin[\frac{\pi}{6}\bar{\theta}])} \tag{11}$$

with $\bar{\sigma}_f = \bar{\sigma}_f[\eta, \bar{\theta}]$ denoting the von Mises equivalent stress at failure as a function of stress state. The corresponding fracture criterion can then be written in the form $\bar{\sigma} \geqslant \bar{\sigma}_f$.

4.2. Mixed Stress/strain-based Mohr–Coulomb (damage indicator) fracture model

For the present plasticity model, a one-to-one relationship between the equivalent plastic strain to fracture, $\bar{\varepsilon}_p^f$, and the von Mises stress to fracture, $\bar{\sigma}_f$, is given by the isotropic hardening law. Assuming that the envelope defined by (11) lies outside of the initial yield surface ($\bar{\sigma}_f \geqslant k[0]$), the equivalent plastic strain to fracture can be expressed as a function of the stress state by combining Eqs. (5) and (11),

$$\bar{\varepsilon}_p^f[\eta, \bar{\theta}] = k^{-1}\left[\frac{c_2}{\sqrt{\frac{1+c_1^2}{3}}\cos(\frac{\pi}{6}\bar{\theta}) + c_1(\eta + \frac{1}{3}\sin(\frac{\pi}{6}\bar{\theta}))}\right]. \tag{12}$$

Using $\bar{\varepsilon} \geqslant \bar{\varepsilon}_p^f[\eta, \bar{\theta}]$ as fracture criterion is fully-equivalent to using the stress-based Mohr–Coulomb fracture model (10).

Here, an empirical damage indicator framework (e.g., Fischer et al., 1995) is used in conjunction with Eq. (12). The onset of fracture is said to occur when a scalar-valued damage indicator function D of initial value zero reaches unity, $D = 1$. The evolution equation for the damage indicator function reads,

$$dD = w[\eta, \bar{\theta}]d\bar{\varepsilon}_p, \tag{13}$$

where the stress-state dependent weighting function $w[\eta, \bar{\theta}]$ is defined through the reciprocal of the fracture strain $\bar{\varepsilon}_p^f[\eta, \bar{\theta}]$,

$$w[\eta, \bar{\theta}] = \frac{1}{\bar{\varepsilon}_p^f[\eta, \bar{\theta}]}. \tag{14}$$

4.3. Model parameter identification

The model parameters are identified based on the results from three notched tensile experiments and the punch test. As illustrated by Fig. 5, these four experiments cover stress triaxialities ranging from 0.4 to 0.66 which is critically important for sheet metal forming. At the same time, the Lode angle parameter varies from −1.0 to 0.9.

4.4. Stress-based model calibration

In the case of the stress-based fracture model, the deterministic parameter identification based on two data points $\{\bar{\sigma}^{(1)}, \eta^{(1)}, \bar{\theta}^{(1)}\}$ and $\{\bar{\sigma}^{(2)}, \eta^{(2)}, \bar{\theta}^{(2)}\}$ leads to the solution

$$\begin{aligned} c_1 &= \frac{\mathrm{sign}(A)}{\sqrt{3A^2 - 1}} \quad \text{with } A: \\ &= \frac{\bar{\sigma}^{(1)}\{\eta^{(1)} + \frac{1}{3}\sin(\frac{\pi}{6}\bar{\theta}^{(1)})\} - \bar{\sigma}^{(2)}\{\eta^{(2)} + \frac{1}{3}\sin(\frac{\pi}{6}\bar{\theta}^{(2)})\}}{-\bar{\sigma}^{(1)}\cos(\frac{\pi}{6}\bar{\theta}^{(1)}) + \bar{\sigma}^{(2)}\cos(\frac{\pi}{6}\bar{\theta}^{(2)})}, \end{aligned} \tag{15}$$

$$c_2 = \bar{\sigma}^{(1)}\left\{\sqrt{\frac{1+c_1^2}{3}}\cos\left[\frac{\pi}{6}\bar{\theta}^{(1)}\right] + c_1\left(\eta^{(1)} + \frac{1}{3}\sin\left[\frac{\pi}{6}\bar{\theta}^{(1)}\right]\right)\right\}$$

along with the constraint

$$A^2 \geqslant 1/3. \tag{16}$$

This constraint implies that the two parameter Mohr–Coulomb model cannot be fitted exactly to any two experimental data points. For instance, for the present material data, condition (16) is not satisfied when choosing the punch experiment along with a notched tensile experiment. The Mohr–Coulomb fracture model can thus only be identified in an approximate manner for the present material. We chose all three notched tensile experiments and the punch experiment for calibration based on the minimization of the cost function

$$\psi[c_1, c_2] = \sum_{i-1}^{4}(k^{-1}[\bar{\sigma}^{(i)}] - \bar{\varepsilon}_p^f[\eta^{(i)}, \bar{\theta}^{(i)}])^2 \tag{17}$$

while

$$(c_1, c_2) = \arg\min(\psi[c_1, c_2]). \tag{18}$$

It is important to determine the cost function in terms of the error in the predicted equivalent plastic strain to fracture. It is more natural to define an error norm in the stress space, e.g.,

$$\tilde{\psi}[c_1, c_2] = \sum_{i-1}^{4}(\bar{\sigma}^{(i)} - \bar{\sigma}_f[\eta^{(i)}, \bar{\theta}^{(i)}])^2 \tag{19}$$

However, due to the asymptotic nature of the function $k[\bar{\varepsilon}_p]$, the minimization problem becomes more accurate from an engineering point of view when using (17) instead of (19). It is also emphasized that the stress-based model calibration is based on the strain to fracture as determined from hybrid experimental-numerical analysis. In other words, there is no need to measure the stress to fracture to determine the parameters of a stress-based fracture criterion for ductile materials. It is actually important not to use measured stresses directly as the predictions of a stress-based fracture model depend strongly on the underlying plasticity model.

After applying the above calibration procedure, we obtained a friction coefficient of $c_1 = 0.32$ and a cohesion of $c_2 = 415MPa$. The measured and predicted fracture strains are listed in Table 2 for all calibration experiments. Based on this calibration, the model overestimates the strain to fracture by 6% for notched tension with $R = 20$ mm, while it underestimates the strain to fracture by 3.6% in the case of the punch experiments. The corresponding error is smaller than 4.1% for the other two notched tension experiments.

4.5. Mixed Stress/strain-based damage indicator model calibration

The model parameter identification of the mixed stress/strain-based damage indicator model requires a full inverse calibration procedure. For given set of parameters (c_1, c_2), we integrate the damage increments according to (13) along the computed experimental loading path for each experiment to determine the predicted strain to fracture as $D = 1$. The cost function given by (17) is then employed to specify the optimization problem for c_1 and c_2. It is worth noting that a calibration constraint similar to Eq. (16) also applies implicitly to the mixed stress/strain-based model, i.e., the 2-parameter model cannot always be fitted exactly to two experiments. For the low carbon steel, the numerical optimization using a derivative-free Nelder-Mead algorithm (Matlab) yields the parameters $c_1 = 0.31$ and $c_2 = 405$ MPa. The comparison of the measured and predicted equivalent plastic strains to fracture reveals errors of up to 11.5% which is about twice as high as for the stress-based model. In other words, the ability of the Mohr–Coulomb model to be fitted to the present experimental data is reduced through the introduction of the damage accumulation framework. However, it is worth noting that the obtained parameters are close to those obtained for the stress-based model which indicates that the damage accumulation framework seems to

Table 2
Measured and predicted strain to fracture of all calibration tests.

	Notch			Punch
	R = 20 mm	R = 10 mm	R = 6.67 mm	
$\bar{\varepsilon}^f_{p,\text{measured}}$ (–)	0.388	0.358	0.357	0.527
$\bar{\varepsilon}^f_{p,\text{stress-based}}$ (–)	0.413	0.373	0.353	0.509
Err (%)	6.0	4.1	−1.3	−3.6
$\bar{\varepsilon}^f_{p,\text{mixed-based}}$ (–)	0.429	0.383	0.357	0.473
Err (%)	9.6	6.6	0.1	−11.5

preserve some of (instead of completely overwriting) the original physical meaning of the original Mohr–Coulomb model for the present calibration experiments. Note that the stress-based and mixed stress/strain-based models are only identical when the stress triaxiality and Lode angle parameters remain constant throughout an experiment.

4.6. Visualization of the calculated fracture functions

The calibration of the stress-based and mixed stress/strain-based fracture models yielded two different sets of (c_1, c_2). However, in the special case of the radial loading, the stress triaxiality and the Lode angle parameter remain constant, and the fracture strain predicted by both models is given by Eq. (12). For visualization purposes, we limit our attention to plane stress states where the equivalent plastic strain to fracture can be represented as a function of the stress triaxiality only due to the relationship

$$\bar{\theta} = 1 - \frac{2}{\pi}\arccos\left[-\frac{27}{2}\eta\left(\eta^2 - \frac{1}{3}\right)\right]. \tag{20}$$

The blue curve in Fig. 7 depicts the envelope for the stress-based model, while the corresponding curve for the mixed stress/strain-based model is depicted in red. The comparison of these two curves reveals that the predicted strain to fracture for proportional loading under plane stress conditions is by about $\Delta\bar{\varepsilon}^p = 0.02$ lower for the strain-based model. The shape of the fracture envelopes shows that the strain to fracture is the same for uniaxial tension and equi-bixial tension along with a minimum for transverse plane strain which is a characteristic feature of the combination of a von Mises yield surface with isotropic hardening and the Mohr–Coulomb fracture model.

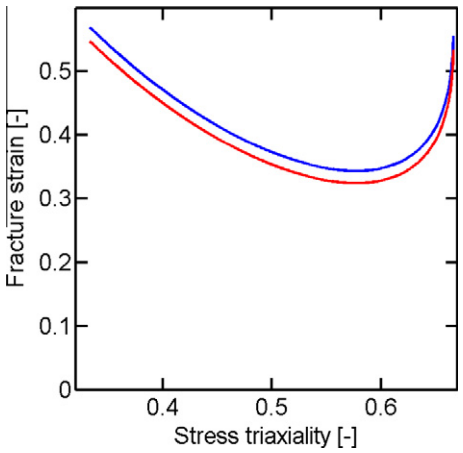

Fig. 7. Comparison of the fracture envelopes for proportional plane stress loading for the stress-based model (red) and mixed stress/strain-based damage indicator model (blue). (For interpretation of the references to colour in this figure legend, the reader is referred to the web version of this article.)

5. Model validation and discussion

5.1. Validation experiments

Two validation experiments are performed. The first is a punch experiment on a Hasek specimen. The disk-shaped Hasek specimen (see deformed specimen in Fig. 6b) features two circular cut-outs of 16 mm radius along with a minimum gage section width of 17 mm. The specimen is extracted such that its tensile axis is aligned with the transverse sheet direction. The same experimental set-up is employed for the Hasek tests as for the above punching experiment (including the stack of four oil-lubricated Teflon layers). The measured force-displacement curve for a punch velocity of 3 mm/min is shown in Fig. 6d. Note that a significantly smaller displacement to fracture is achieved than in the punch experiment.

The second validation experiment is the stamping of an anti-clastic structure with a set of two male dies. This particular stamping experiment is chosen because it features severely strained zones under equi-biaxial tension and transverse plane strain tension. Furthermore, it can be performed without using a blank holder. The bottom die features a square array of 25 pins, while the top die comprises only 16 pins. The pins have a diameter of 9.2 mm while a pin spacing of D = 13.5*mm* is used. A flat specimen of the size 70x70 mm is used in this experiment. A thin layer of grease has been applied to the sheet and the dies to reduce friction. Throughout the experiment, the top die moves downward at a constant velocity of 2 mm/min. A 250kN load cell is used to record the total vertical force along with the position of the cross-head. Fig. 8a shows the recorded force-displacement curve for the stamping experiment. The experiment on a second specimen has been interrupted at a cross-head displacement of 5.9 mm for optical inspection. While two small cracks are visible at a displacement of 6.0 mm, no cracks are visible at a magnification of 10x on a stereo microscope for a displacement of 5.9 mm. The cracks are located in the unsupported region between two neighboring upwardly and downwardly pointing pins (Fig. 9).

5.2. Modeling of the validation experiments

The numerical model of the Hasek test is built in close analogy with the model for the punch experiments (about the same element size and also eight solid elements along the thickness direction; friction coefficient of 0.04). The comparison of the measured and computed force-displacement curves (Fig. 6d) indicates very good agreement. The computed loading path in terms of equivalent plastic strain versus Lode angle and stress-triaxiality is shown in Fig. 5. Observe that the loading path for the Hasek test covers a similar range of stress states as the notched tensile experiments. The hybrid-experimental analysis reveals an equivalent plastic strain to fracture of 0.36. The mixed stress/strain-based model predicts a strain to fracture of 0.38 while the stress-based model yields an estimate of 0.37.

As far as the stamping validation experiment is concerned, only one quarter of the sheet is modeled using symmetry boundary conditions. In the computational model, each the top and bottom die comprise four punches which are modeled as analytical rigid surfaces with a friction coefficient of 0.06. A solid element mesh is employed representing the sheet material with eight elements along the thickness direction. The mesh is refined near the center of the specimen where the deformation is most severe. A total of 180,000 eight-node first-order solid elements are employed. More than 100,000 explicit time steps are performed to perform the stamping simulation up to the point of onset of fracture. Fig. 9 compares the predicted and measured force-displacement curves (for a machine stiffness of 200kN/mm). Observe the much lower

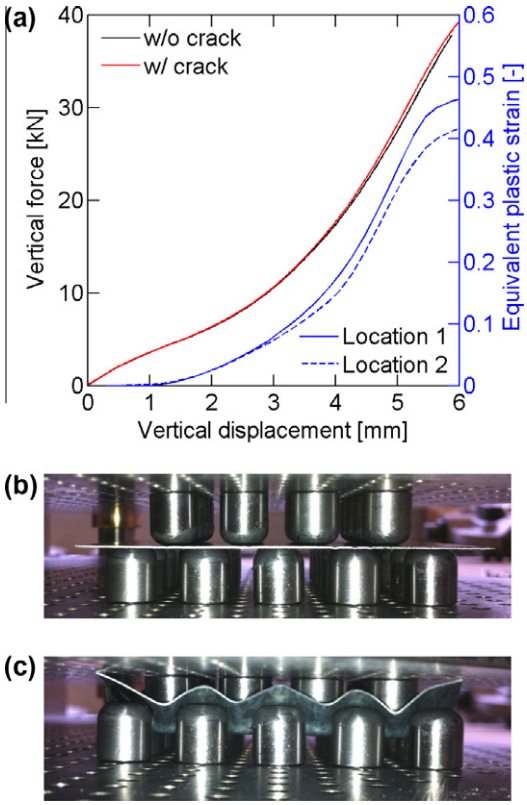

Fig. 8. Stamping experiment: (a) force-displacement curve (primary axis) and evolution of the equivalent plastic strain (secondary axis); side view of the experimental set-up showing (b) the initial configuration, and (c) an intermediate configuration.

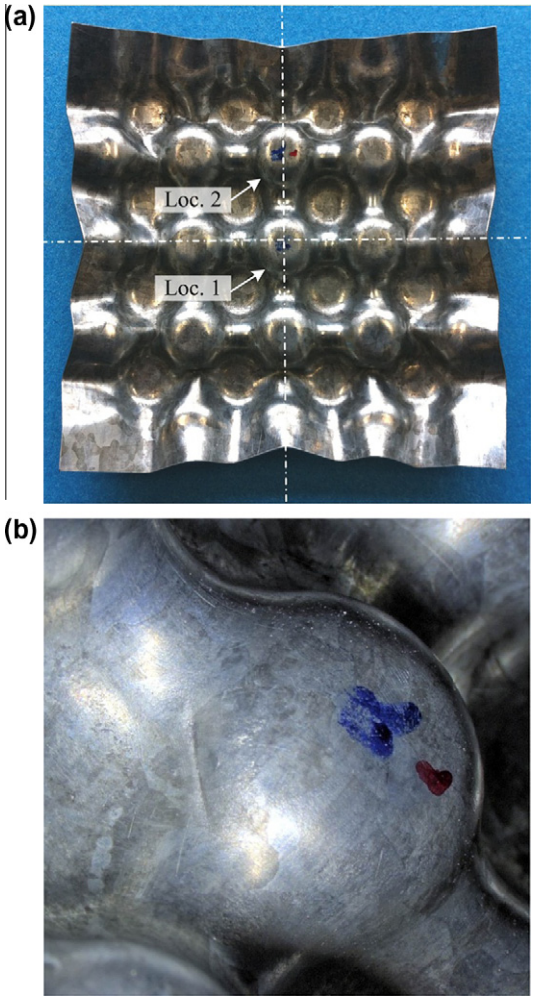

Fig. 9. Sheet specimen after stamping all the way to fracture: (a) top view, (b) close-up of the crack observed at location #2.

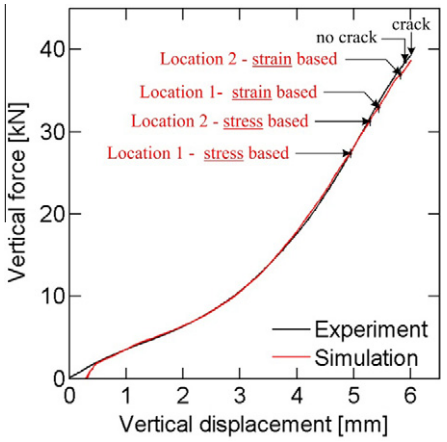

Fig. 10. Comparison of the model predictions with the experimentally measured force–displacement curve for stamping; the labels with arrows indicate the instant of onset of fracture as predicted by the stress- and mixed stress/strain-based fracture models.

apparent initial slope of the experimental curve. This difference is attributed to small geometric imperfections in the experimental set-up which cause the non-uniform initial loading of the specimen. This effect is significant in the elastic range, but negligible thereafter (see Fig. 10).

Both the mixed stress/strain-based and stress-based models underestimate the displacement to fracture. According to the mixed stress/strain-based model, fracture is expected at a displacement of 5.4 mm at a first location and at a displacement of 5.8 mm at a second location. These two locations are highlighted in Fig. 11. They coincide with the locations of the cracks observed in the experiment (Fig. 9). Note that the cracks form on the tensile side of a region of two positive curvatures. The stress-based model predicts fracture at the same locations, but much earlier. The predicted displacements to fracture for the stress-based model are 4.9 mm and 5.3 mm for locations 1 and 2, respectively.

The loading paths to fracture for location #1 are shown in Figs 5a and b. It is highly non-linear and covers a remarkably wide range of stress states. As compared to the loading paths for all other experiments, an increment in displacement causes only a small increase in the equivalent plastic strain (Fig 8b) towards the end of the experiment, but a substantial change in stress state. The stamping experiment therefore provides a good resolution as far as the identification of the strain to fracture is concerned. The substantial changes in stress state are due to the fact the specimen geometry changes significantly throughout loading. At the same time, the modest increase in plastic strain (with displacement) indicates that the location of fracture initiation is not located inside a neck that accommodates all plastic deformation. It is also worth noting that the use of fracture models that express the strain to fracture as a smooth continuous function of the stress triaxiality only would probably not be able to predict the fracture with reasonable accuracy. This can be seen from Fig. 5a. Suppose a fracture envelope that connects the end

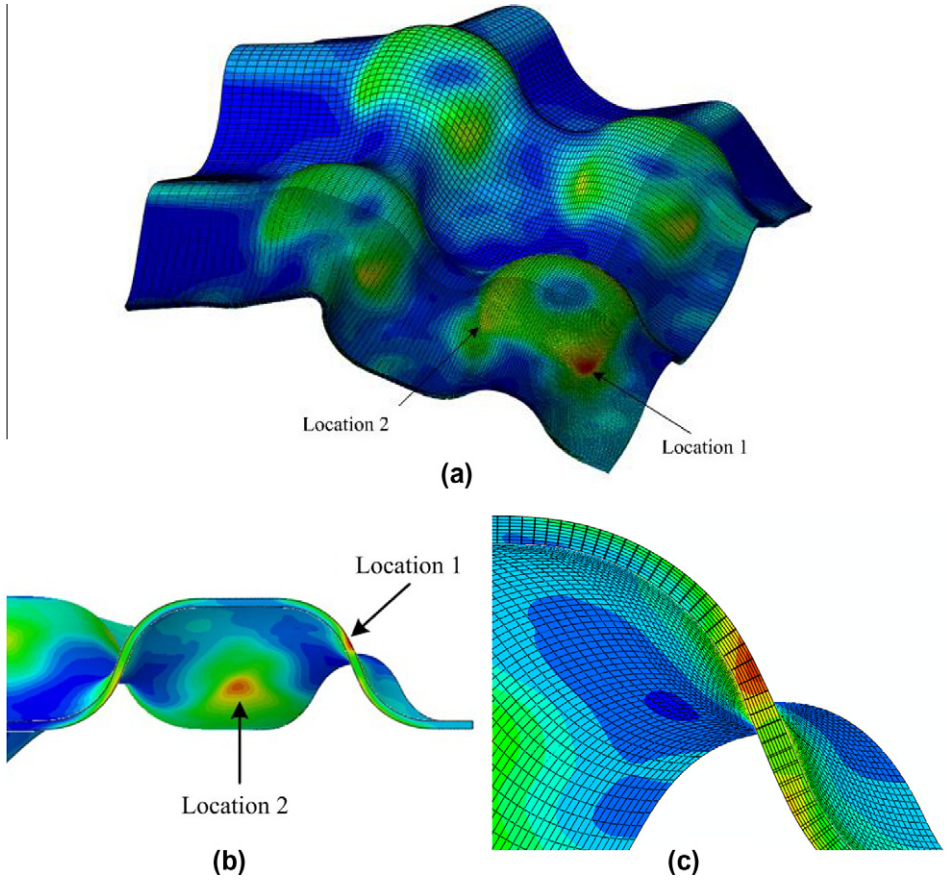

Fig. 11. Deformed FE mesh for stamping with contours of the damage indicator, (a) 3D view, and (b) side view of the quarter model, (c) detail of location 1 with the equivalent plastic strain as contour.

points of the loading paths for all punch experiments (shown as thin dashed line in Fig. 5a). The loading path for stamping would intersect this hypothetical envelope at an early stage of loading. It thus appears to be important to incorporate the effect of the Lode angle in the fracture model.

5.3. Comment on the effect of the loading path

The results of our hybrid experimental-numerical analysis suggest that the Mohr–Coulomb model provides more accurate predictions when embedded in the damage indicator framework as compared to the direct use of its original stress-based form. Besides this apparent advantage, the mixed stress/strain-based damage indicator model formulation also appears to be more sound from a conceptual point of view.

For illustration, we limit our attention to plane stress conditions and plot the stress-based fracture criterion in stress-space (Fig. 12). We also limit our discussions to stress states between uniaxial tension and equi-biaxial tension. The initial yield surface is depicted as a solid black curve with the label $\bar{\varepsilon}_p = 0$. In addition, dashed black lines represent the yield envelopes for $\bar{\varepsilon}_p = 0.34$ (fracture strain for transverse plane strain tension), an intermediate strain of $\bar{\varepsilon}_p = 0.45$ and the fracture strain for equi-biaxial tension ($\bar{\varepsilon}_p = 0.55$). The calibrated Mohr–Coulomb fracture envelope is shown as a solid blue line. Note that the solution of Eq. (10) depends on the minimum and maximum principal stress only. For plane stress tension, the smallest principal stress is always zero and thus the Mohr–Coulomb model reduces to a maximum principal stress criterion, i.e., the blue envelope drawn in Fig. 12 corresponds to two perpendicular straight lines.

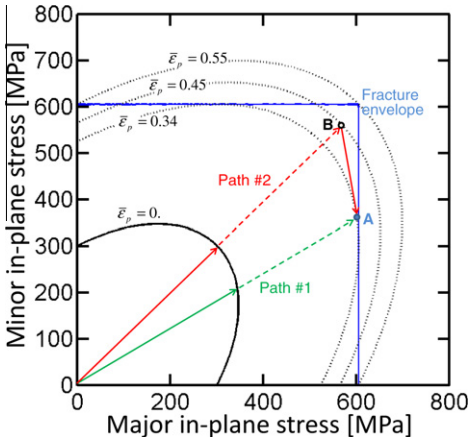

Fig. 12. Illustration of two distinct loading paths in stress space. The black envelopes correspond to different levels of equivalent plastic strain; the blue curve highlights the fracture envelope in stress space for plane stress conditions.

Now consider two distinct loading paths:

(1) The first is a monotonic radial loading path in stress space (green) which involves elastic loading (solid green line) followed by elasto-plastic loading (dashed green line) all the way to fracture at an equivalent plastic strain of $\bar{\varepsilon}_p = 0.34$ (point A).

(2) The second loading path (red) involves elastic and elasto-plastic monotonic radial loading up to an equivalent plastic strain of $\bar{\varepsilon}_p = 0.45$ (point B). Subsequently, the direction of loading is changed and a linear loading path is assumed up to point A.

Observe that the second portion of loading path #2 lies entirely in the elastic domain defined by the yield envelope for $\bar{\varepsilon}_p = 0.45$. According to the stress-based fracture model, fracture would occur at point A for both loading paths. This is due to the full path independency of the stress-based fracture model in stress space. However, the model predictions are path dependent in the space $\{\bar{\varepsilon}_p, \eta, \bar{\theta}\}$. Note that the equivalent plastic strain to fracture after loading path #2 is $\bar{\varepsilon}_p^{f(\#2)} = 0.45$, while a strain to fracture of only $\bar{\varepsilon}_p^{f(\#1)} = 0.34$ is reached after loading path #1.

A mixed stress/strain-based damage indicator model using the same set of parameters c_1 and c_2 as the stress-based model would also predict fracture at point A after loading path #1. However, the material would still be intact according to the damage accumulation rule after loading path #2. There is no damage accumulation possible if the loading path is purely elastic. Thus, the value of the damage indicator would be the same at points A and B ($D_A = D_B < 1$). Thus, the material could still be strained further plastically at point B after loading path #2. In other words, the strain to fracture under transverse plane strain conditions after loading path #2 would not only exceed $\bar{\varepsilon}_p^{f(\#1)} = 0.34$, but also exceed the strain of $\bar{\varepsilon}_p^{f(\#2)} = 0.45$ which had been predicted by the stress-based model. At this point, we cannot fully assess the validity of either model assumption due to the lack of comprehensive experimental data. However, the possible prediction of fracture in the elastic domain is an undesirable (but obvious) feature of the stress-based model which is traditionally used for brittle materials.

6. Conclusions

In the present work, attention is limited to tension-dominated stress states in sheet metal forming between uniaxial tension and equi-biaxial tension. A hybrid experimental-numerical program is carried out on thin low carbon steel sheets involving notched tension tests, a punch experiment for equi-biaxial tension, a Hasek test and a stamping experiment. The deformation behavior of the low carbon steel is modeled using a non-associated plasticity with a von Mises yield surface and a planar orthotropic Hill'48 flow rule. Two different implementations of the two-parameter Mohr–Coulomb failure model are employed. The stress-based version corresponds to the original Mohr–Coulomb model which describes a failure surface in stress space. The mixed stress/strain-based version corresponds to a damage indicator model where the stress-state dependent weighting function is derived from the transformation of the Mohr–Coulomb model into the space of stress triaxiality, Lode angle parameter and equivalent plastic strain. Both models could be calibrated with good accuracy based on the results from the punch and three notched tension tests. This is attributed to the fact that the Mohr–Coulomb fracture model captures the decrease in ductility for transverse plane strain tension with respect to uniaxial tension and equi-biaxial tension when it is used in conjunction with the von Mises yield surface. The subsequent application of the calibrated models to predict the onset of fracture during the stamping of an anticlastic structure reveals a much higher prediction accuracy of the mixed stress/strain-based version as compared to the stress-based formulation.

Acknowledgements

The authors are grateful to Stephane Marcadet (MIT/Ecole Polytechnique) and Matthieu Dunand (MIT/Ecole Polytechnique) for their help with the experiments.

References

Bai, Y., Wierzbicki, T., 2008. A new model of metal plasticity and fracture with pressure and Lode dependence. Int. J. Plast. 24, 1071–1096.
Bai, Y., Wierzbicki, T., 2010. Application of extended Mohr–Coulomb criterion to ductile fracture. Int. J. Fract. 161, 1–20.
Bao, Y., Wierzbicki, T., 2004a. A comparative study on various ductile crack formation criteria. J. Eng. Mater. Technol. 126, 314–324.
Bao, Y.B., Wierzbicki, T., 2004b. On fracture locus in the equivalent strain and stress triaxiality space. Int. J. Mech. Sci. 46 (1), 81–98.
Barsoum, I., Faleskog, J., 2007. Rupture Mechanisms in Combined Tension and Shear – Experiments. Int. J. Solids Struct. 44 (6), 1768–1786.
Benzerga, A., Leblond, J.B., 2010. Ductile fracture by void growth to coalescence. Adv. Appl. Mech. 44, 169–305.
Benzerga, A.A., Besson, J., Pineau, A., 2004. Anisotropic ductile fracture Part II: theory. Acta Mater. 52, 4639–4650.
Besson, J., 2010. Continuum models of ductile fracture: a review. Int. J. Damage Mech. 19 (1), 3–52.
Bigoni, D., Piccolroaz, A., 2004. Yield criteria for quasibrittle and frictional materials. Int. J. Solids Struct. 41, 2855–2878.
Borvik, T., Dey, S., Clausen, A.H., 2009. Perforation resistance of five different high-strength steel plates subjected to small-arms projectiles. Int. J. Impact Eng. 36 (7), 948–964.
Brozzo, P., Deluca, B., Rendina, R., 1972. A new method for the prediction of formability in metal sheets, sheet material forming and formability. In: Proceedings of the 7th biennial Conference of the IDDRG, 1972.
Chu, C.C., Needleman, A., 1980. Void nucleation effects in biaxially stretched sheets. J. Eng. Mater. Technol. 102 (3), 249–256.
Clift, S.E., Hartley, P., Sturgess, C.E.N., Rowe, G.W., 1990. Fracture prediction in plastic deformation processes. Int. J. Mech. Sci. 32, 1–17.
Cockcroft, M.G., Latham, D.J., 1968. Ductility and the workability of metals. J. Inst. Met. 96, 33–39.
Coppola, T., Cortese, L., Folgarait, P., 2009. The effect of stress invariants on ductile fracture limit in steels. Eng. Fract. Mech. 76 (9), 1288–1302.
Cvitanic, V., Vlak, F., Lozina, Z., 2008. A finite element formulation based on non-associated plasticity for sheet metal forming. Int. J. Plast. 24, 646–687.
Danas K, Ponte Castaneda P, A finite-strain model for anisotropic viscoplastic porous media: I - Theory. Eur. J. Mech. A/Solids 28, 387–401, 2009a.
Danas, K., 2009b. Ponte Castaneda P, A finite-strain model for anisotropic viscoplastic porous media: II - Applications. Eur. J. Mech. A/Solids 28, 402–416.
Danas, K., 2012. Ponte Castañeda P, Influence of the Lode parameter and the stress triaxiality on the failure of elasto-plastic porous materials. Int. J. Solids Struct.. http://dx.doi.org/10.1016/j.ijsolstr.2012.02.006.
Danas, K., Idiart, M.I., Ponte Castaneda, P., 2008. Homogenization-based constitutive model for isotropic viscoplastic porous media. Int. J. Solids Struct. 45, 3392–3409.
Dunand, M., Mohr, D., 2010. Hybrid experimental-numerical analysis of basic ductile fracture experiments for sheet metals. Int. J. Solids Struct. 47, 1130–1143.
Dunand, M., Mohr, D., 2011. On the predictive capabilities of the shear modified Gurson and the modified Mohr–Coulomb fracture models over a wide range of stress triaxialities and Lode angles. J. Mech. Phys. Solids 59 (7), 1374–1394.
Fagerholt, E., Dorum, C., Borvik, T., Laukli, H.I., Hopperstad, O.S., 2010. Experimental and numerical investigation of fracture in a cast aluminium alloy. Int. J. Solids and Structures 47 (24), 3352–3365.
Fischer, F.D., Kolednik, O., Shan, G.X., Rammerstorfer, F.G., 1995. A note on calibration of ductile failure damage indicators. Int. J. Fract. 73 (4), 345–357.
Garajeu, M., Michel, J.C., Suquet, P., 2000. A Micromechanical Approach of Damage in Viscoplastic Materials by Evolution in Size. Shape and Distribution of Voids, Computer Methods in Applied Mechanics and Engineering 183 (3–4), 223–246.
Gologanu, M., Leblond, J.B., Devaux, J., 1993. Approximate models for ductile metals containing nonspherical voids – case of axisymmetrical prolate ellipsoidal cavities. J. Mechs. Phys. Solids 41 (11), 1723–1754.
Gologanu, M., Leblond, J.B., Devaux, J., 1994. Approximate models for ductile metals containing nonspherical voids – case of axisymmetrical oblate ellipsoidal cavities. J. Eng. Mater. Technol. 116 (3), 290–297.
Gurson, A.L., 1977. Continuum Theory of Ductile Rupture by Void Nucleation and Growth: Part I-Yield Criteria and Flow Rules for Porous Ductile Media. J. Eng. Mater. Technol. 99, 2–15.
Hancock, J.W., Mackenzie, A.C., 1976. On the mechanisms of ductile fracture in high-strength steels subject to multi-axial stress states. J. Mech. Phys. Solids 24, 147–160.
Hill, R., 1952. On discontinuous plastic states, with special reference to localized necking in thin sheets. Int. J. Mech. Phys. Solids 1, 19–30.
Johnson, G.R., Cook, W.H., 1985. Fracture characteristics of three metals subject to various strains, strain rates, temperatures and pressures. Engng. Fract. Mech. 21, 31–48.
Keeler, S.P., Backofen, W.A., 1963. Plastic instability and fracture in sheets stretched over ridgig punches. Trans. ASM 56, 25–48.
Khan, A.S., Liu, H., 2012. A new approach for ductile fracture prediction on Al 2024–T351 alloy. Int. J. Plast 35, 1–12.
Kleemola, H.J., Pelkkikangas, M.T., 1977. Effect of predeformation and strain path on the forming limits of steel, copper, and brass. Sheet Metal Indus. 63, 591–599.
Lassance, D., Fabregue, D., Delannay, F., Pardoen, T., 2007. Micromechanics of room and high temperature fracture in 6xxx Al alloys. Prog. Mater Sci. 52, 62–129.

Leblond, J.B., Perrin, G., Devaux, J., 1995. An improved Gurson-type model for hardenable ductile metals. Eur. J. Mech. A-Solids 14 (2), 499–527.
Lemaitre, J., 1985. A continuous damage mechanics model for ductile fracture. J. Eng. Mater. Technol. 107, 83–89.
LeRoy, G., Embury, J.D., Edward, G., Ashby, M.F., 1981. A model of ductile fracture based on the nucleation and growth of voids. Acta Metall. 29, 1509–1522.
Li, H., Fu, M.W., Lua, J., Yang, H., 2011. Ductile fracture: experiments and computations. Int. J. Plast 27, 147–180.
Lode, W., 1926. Versuche über den Einfluß der mittleren Hauptspannung auf das Fließen der Metalle Eisen. Kupfer und Nickel, Zeitschrift für Physik 36 (11–12), 913–939.
Malcher, L., Andrade Pires, F.M., César de Sá, J.M.A., 2012. An assessment of isotropic constitutive models for ductile fracture under high and low stress triaxiality. Int. J. Plast. 30–31, 81–115.
Marciniak, Z., Kuczynski, K., 1967. Limit strains in the processes of stretch forming sheet steel. J. Mech. Phys. Solids 1, 609–620.
McClintock, F.A., 1968. A criterion of ductile fracture by the growth of holes. J. Appl. Mech. 35, 363–371.
Mohr, O., 1900. Welche Umstaende bedingen die Elastizitaetsgrenze und den Bruch eines Materials. Zeitschrift des Vereins Deutscher Ingenieure 44, 1524–1530.
Mohr, D., Dunand, M., Kim, K.H., 2010. Evaluation of associated and non-associated quadratic plasticity models for advance high strength steel sheets under multi-axial loading. Int. J. Plast. 26, 939–956.
Nahshon, K., Hutchinson, J.W., 2008. Modification of the Gurson model for shear fracture, Eur. J. Mech./A Solids 27, 1–17.
Nielsen, K.L., Tvergaard, V., 2010. Ductile shear failure of plug failure of spot welds modeled by modified Gurson model. Eng. Fract. Mech. 77, 1031–1047.
Oh, S., Chen, C.C., Kobayashi, S., 1979. Ductile failure in axisymmetric extrusion and drawing, Part 2: Workability in Extrusion and Drawing. J. Eng. Ind. 101, 36–44.
Pardoen, T., Hutchinson, J.W., 2000. An extended model for void growth and coalescence. J. Mech. Phys. Solids 48 (12), 2467–2512.
Ponte Castaneda, P., Zaidman, M., 1994. Constitutive models for porous materials with evolving microstructure. J. Mech. Phys. Solids 42, 1459–1497.
Rice, J.R., Tracey, D.M., 1969. On the ductile enlargement of voids in triaxial stress fields. J. Mech. Phys. Solids 17, 201–217.
Stoughton, T.B., 2000. General forming limit criterion for sheet metal forming. Int. J. Mech. Sci. 42, 1–27.
Stoughton, T.B., Yoon, J.W., 2004. A pressure-sensitive yield criterion under a non-associated flow rule for sheet metal forming. Int. J. Plast. 20, 705–731.
Stoughton, T.B., Yoon, J.W., 2011. A new approach for failure criterion for sheet metals. Int. J. Plast. 27, 440–459.
Swift, H.W., 1952. Plastic instability under plane stress. J. Mech. Phys. Solids 1, 1–16.
Tvergaard, V., Needleman, A., 1984. Analysis of the cup–cone fracture in a round tensile bar. Acta Metall. 32, 157–169.
Wierzbicki, T., Bao, Y., Lee, Y.W., Bai, Y., 2005. Calibration and evaluation of seven fracture models. Int. J. Mech. Sci. 47, 719–743.
Xue, L., 2008. Constitutive modeling of void shearing effect in ductile fracture of porous materials. Eng. Fract. Mech. 75, 3343–3366.
Xue, Z., Faleskog, J., Hutchinson, J.W., submitted. Tension–torsion fracture experiments—Part II: Simulations with the extended Gurson model and a ductile fracture criterion based on plastic strain.